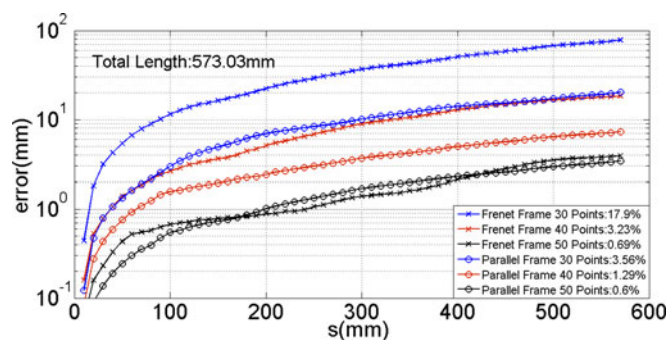


# Parallel Transport Frame for Fiber Shape Sensing

Volume 10, Number 1, February 2018

Jiwen Cui  
Shiyuan Zhao  
Chaoqiang Yang  
Jiubin Tan



DOI: 10.1109/JPHOT.2017.2782736

1943-0655 © 2018 IEEE

# Parallel Transport Frame for Fiber Shape Sensing

Jiwen Cui, Shiyuan Zhao , Chaoqiang Yang, and Jiubin Tan

Center of Ultra-precision Optoelectronic Instrument, Harbin Institute of Technology, Harbin 150080, China

DOI:10.1109/JPHOT.2017.2782736

1943-0655 © 2018 IEEE. Translations and content mining are permitted for academic research only.

Personal use is also permitted, but republication/redistribution requires IEEE permission.

See [http://www.ieee.org/publications\\_standards/publications/rights/index.html](http://www.ieee.org/publications_standards/publications/rights/index.html) for more information.

Manuscript received August 12, 2017; revised November 25, 2017; accepted December 8, 2017. Date of publication December 12, 2017; date of current version February 7, 2018. This work was supported in part by the National Natural Science Foundation of China under Grant 51575140 and in part by the Youth Talents Foundation of Harbin under Grant RC2016JQ006007. Jiwen Cui and Shiyuan Zhao contributed equally to this work. Corresponding author: Jiwen Cui (e-mail: cuijiwen@hit.edu.cn).

**Abstract:** This paper reports a reconstruction method to determine a 3-D space curve from the distributed strain by using the parallel transport frame. Parallel transport frame can efficiently eliminate the singularities and discontinuous point which appear in another existing commonly used reconstruction method Frenet Frame and thus improve the accuracy and stability of the shape sensing. To validate this method, a simulation method based on the rotation minimizing frame is proposed and used. It provides a general procedure to numerically obtain the strain distribution with a certain configuration of the shape sensor and spatial shape. Some typical space curves whose space position is analytically given are reconstructed by two reconstruction methods and the results are compared. The error sources of the reconstruction method are also analyzed.

**Index Terms:** Fiber optics systems, sensors.

## 1. Introduction

Three-Dimensional shape sensing is essential in a wide range of applications including soft robotics, medical needle bending deflection measurement and human body monitoring [1]–[3]. Fiber optics technique is especially considered as a promising candidate and high-efficient technique for shape sensing in these areas. Various approaches and shape sensors based on the fiber optics have been proposed in recent years. The multi-core optical fibers and substrate-attaching-fibers are two main forms of the fiber shape sensor [4], [5]. The strain along the fiber is interrogated by OFDR or WDM system according to different sensing principles, FBG arrays or Rayleigh scatter [6]–[8]. The fiber shape can then be reconstructed according to different theories, which depend on the certain application: linear cantilever beam theory for biopsy needles [9] or Frenet Frame for endoscopes and other flexible instruments [10]–[12]. For all these applications, a reconstruction algorithm directly affects the accuracy and stability of the shape sensing. For a flexible structure, Frenet Frame is the mostly used reconstruction method. However, Frenet Frame suffers singularities when the curve changes direction [13] and is discontinuous when a local line exists. The Frenet Frame before and after the zero-curvature position can be entirely different, so it's hard to define a unique continuous Frenet Frame over the whole curve [14]. This problem limits improvement of the accuracy and leads to the failure of the reconstruction.

In this paper, the Parallel transport frame is introduced and used to reconstruct the shape of the fiber shape sensor for the first time. We compared the Parallel-transport frame and Frenet Frame and demonstrated how to avoid the bad influence caused by the singularities and local line. Besides, a mathematical tool called rotation minimizing frame (RMF) is also introduced and developed as a method to simulate the distributed strain along the fiber. This method provides a general procedure to numerically obtain the strain distribution with a certain configuration of the shape sensor and spatial shape. It helps us to analyze the reconstruction algorithm without the influence of other errors. The reconstruction result is then evaluated by the deviation between the input shape and the reconstructed shape. Furthermore, with the help of this proposed simulation method, we can investigate the influence of some parameters to the reconstruction conveniently such as the shape which will be constructed, the number of sampled strain along the fiber, or the configuration of the fiber shape sensor. So it can be used as a tool to guide the design of the shape sensor. Three groups of simulation are implemented to make a further demonstration of the reconstruction method. The simulation results show that the Parallel transport frame is more accurate and stable than Frenet Frame when the curve has singularities and local line segment especially at the situation that the sampled strain points are less.

Although the Parallel transport frame and RMF are mathematical methods and are mainly applied in the computer graphics, to our best knowledge, they have not been applied on the fiber shape sensing so far. Next we will demonstrate them in detail. Section 2 compares two reconstruction methods (Frenet and Parallel transport frame) mathematically. Section 3 describes the curve reconstruction process using the Parallel-transport frame from the strain fields. Section 4 describes the method which is developed from the RMF to simulate strain on the fiber. A few typical fiber shapes (cylindrical spiral, curve with local line, sinusoidal curve) are reconstructed and the reconstruction errors of the two methods are analyzed.

## 2. Parallel-Transport Curve Framing

The Parallel transport frame (Parallel Frame) was first proposed by Bishop in 1975 [15]. A curve which is 2-times continuously differentiable in three-dimensional space can be represented as

$$\vec{p}(s) = x(s)\vec{i} + y(s)\vec{j} + z(s)\vec{k}, \quad (1)$$

where  $s$  represents the length along the curve. The Parallel Frame is composed of a tangent vector and two normal vectors at each point along the curve. The tangent unit vector  $\vec{T}(s)$  is defined as

$$\vec{T}(s) = \frac{d\vec{p}(s)}{ds} = \frac{x'(s)\vec{i} + y'(s)\vec{j} + z'(s)\vec{k}}{\sqrt{(x'(s))^2 + (y'(s))^2 + (z'(s))^2}}. \quad (2)$$

Two normal unit vectors  $\vec{N}_1(s)$  and  $\vec{N}_2(s)$  are two vectors perpendicular to  $\vec{T}(s)$  in the normal plane.  $\vec{T}(s)$ ,  $\vec{N}_1(s)$  and  $\vec{N}_2(s)$  obey the differential Equation (3) [15]. According to the theory of

$$\begin{bmatrix} \vec{T}' \\ \vec{N}_1' \\ \vec{N}_2' \end{bmatrix} = \begin{bmatrix} 0 & \kappa_1 & \kappa_2 \\ -\kappa_1 & 0 & 0 \\ -\kappa_2 & 0 & 0 \end{bmatrix} \begin{bmatrix} \vec{T} \\ \vec{N}_1 \\ \vec{N}_2 \end{bmatrix} \quad (3)$$

differential geometry, the direction of vector  $\vec{T}'(s)$  is the bending direction of the space curve. The curvature  $\kappa(s)$  is defined by

$$\kappa(s) = \left| \vec{T}'(s) \right|. \quad (4)$$

According to Equations (3) and (4) we can get

$$\kappa(s) = \sqrt{(\kappa_1(s))^2 + (\kappa_2(s))^2}. \quad (5)$$

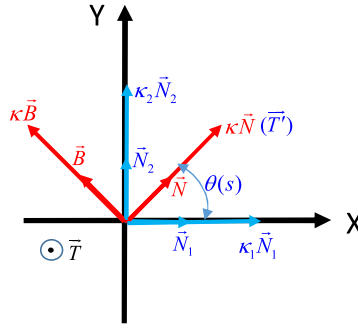


Fig. 1. The geometry relationship between the Frenet Frame and the Parallel Frame.

$\kappa_1(s)$  and  $\kappa_2(s)$  are two components of  $\kappa(s)$  in the direction of  $\vec{N}_1(s)$  and  $\vec{N}_2(s)$ .

$$\theta(s) = \arctan\left(\frac{\kappa_2(s)}{\kappa_1(s)}\right) \quad (6)$$

is the angle between the bending direction  $\vec{T}'(s)$  and  $\vec{N}_1(s)$ .

We compare the Parallel Frame with another existing commonly used reconstruction method called Frenet Frame. The Frenet Frame of a curve is defined by tangent vector  $\vec{T}$ , normal vector  $\vec{N}$ , and binormal vector  $\vec{B}$  at each point of the curve. And they have a relationship as Equation (7).

$$\begin{bmatrix} \vec{T}' \\ \vec{N}' \\ \vec{B}' \end{bmatrix} = \begin{bmatrix} 0 & \kappa & 0 \\ -\kappa & 0 & \tau \\ 0 & -\tau & 0 \end{bmatrix} \begin{bmatrix} \vec{T} \\ \vec{N} \\ \vec{B} \end{bmatrix} \quad (7)$$

$\kappa(s)$  and  $\tau(s)$  are the curvature and torsion of the curve. They are respectively defined as

$$\kappa = \frac{|\vec{p}' \times \vec{p}''|}{|\vec{p}'|^3} \quad \text{and} \quad \tau = \frac{(\vec{p}' \times \vec{p}'') \cdot \vec{p}'''}{|\vec{p}' \times \vec{p}''|^2}. \quad (8)$$

Fig. 1 shows the geometry and the parameter relationship between the Frenet Frame and the Parallel Frame.

Frenet Frame requires that the curve is 3-times continuously differentiable [15]. When there is a singularity or a segment of the local line where  $\vec{p}''(s) = 0$  or  $\vec{T}_i = \vec{T}_{i+1}$ , then there is no locally-determinable coordinate frame component in the plane normal to  $\vec{T}_i$  [16]. In contrast, the Parallel Frame just requires the curve 2-times continuously differentiable. What's more,  $\vec{N}_1(s)$  and  $\vec{N}_2(s)$  depend only on  $\vec{T}(s)$  and not each other [15].  $\vec{N}_1(s)$  and  $\vec{N}_2(s)$  vary smoothly throughout the path regardless of the curve therefore the curve can be defined continuously [16].

### 3. Curve Reconstruction

#### 3.1 Curve Reconstruction

Here we use the shape sensor with a configuration of three fibers symmetrically distributed outside the center line to demonstrate the process of the shape reconstruction by Parallel Frame. Fig. 2 describes the cross-sectional layout of a typical symmetric tri-core fiber which was same with the configuration described in reference [10]. The local coordinate system in each cross section is  $xyz$ .  $\theta_i$  is the angular offset from the  $i$ -th fiber core to the local  $x$  axis.  $\theta_b$  is the angular offset from the fiber bending direction to the local  $x$ -axis.  $d_i$  is the vertical distance from the  $i$ -th outer fiber core to the neutral axis.  $r_i$  is the distance from the  $i$ -th outer fiber core to the center of the sensor. A general

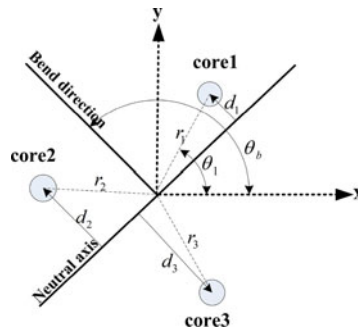


Fig. 2. Typical symmetric tri-core geometry and parameters for determining strain due to bending.

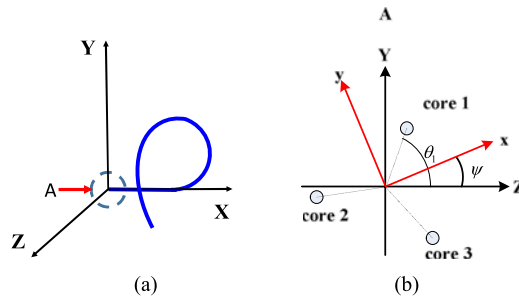


Fig. 3. (a) The fiber shape sensor in the laboratory coordinate system XYZ. (b) The cross side from the perspective A. The sensor consists of three outer cores.

expression for strain in a given core due to bending is

$$\varepsilon_i = -\kappa r_i \cos(\theta_b - \theta_i) \quad (9)$$

For the particular case of a symmetrical core distribution, e.g., symmetrically arranged tri-core fiber, in which cores are equally separated by a  $2\pi/3$  angular offset at the same radial distance from the fiber center, the strain is translated to the curvature through Equation (10).

$$\begin{aligned} \kappa_x &= \kappa \cos \theta_b = -\frac{2}{3} \sum_{i=1}^3 \frac{\varepsilon_i}{r_i} \cos \theta_i \\ \kappa_y &= \kappa \sin \theta_b = -\frac{2}{3} \sum_{i=1}^3 \frac{\varepsilon_i}{r_i} \sin \theta_i \end{aligned} \quad (10)$$

$\kappa_x$  is the curvature component in the x direction and  $\kappa_y$  is the curvature component in the y direction. After interpolation to  $\kappa_x$  and  $\kappa_y$  along the fiber, we can get the discrete coefficient  $\kappa_1(s_j)$  and  $\kappa_2(s_j)$  in the Equation (3). Then Equation (3) can be solved and  $\vec{T}$  is obtained. The deviation of Equation (10) is described in detail in the Appendix.

On the contrary, the bending angle  $\theta_b$  has to be derived to calculate torsion  $\tau(s)$  when using Frenet Frame as demonstrated in reference [10]. The solving may fail when there is a singularity or the line.

### 3.2 Initial Value of the Frame

As shown in Fig. 3, we set up the laboratory coordinate system XYZ and fiber local coordinate system xyz. The position of the fiber with blue color in the laboratory coordinate system is shown in Fig. 3(a) and the cross side from side A is shown in Fig. 3(b).  $\psi$  is the angular offset between

the axis Y, Z in the laboratory coordinate and x, y in the local coordinate system at the initial cross section. The initial value of  $\vec{N}_1(s)$  and  $\vec{N}_2(s)$  can be chosen arbitrarily in the local coordinate xyz. We can make them coincide with x and y respectively. Therefore, in the laboratory coordinate system, the initial value of  $\vec{N}_1(s)$  and  $\vec{N}_2(s)$  are respectively

$$\begin{aligned}\vec{N}_{10} &= [0 \sin \psi \cos \psi], \\ \vec{N}_{20} &= \left[ 0 \sin \left( \psi + \frac{\pi}{2} \right) \cos \left( \psi + \frac{\pi}{2} \right) \right].\end{aligned}\quad (11)$$

For the simplicity in computation, the initial direction of the fiber is along the X axis in the laboratory coordinate system so  $\vec{T}_0$  is (1 0 0). Then three initial values  $\vec{T}_0$ ,  $\vec{N}_{10}$ ,  $\vec{N}_{20}$  and curvatures  $\kappa_1(s_j)$ ,  $\kappa_2(s_j)$  along the fiber are substituted into Equation (3).  $\vec{T}$  can be obtained by solving Equation (3). The whole fiber position vectors can be calculated by

$$\vec{p}(s) = \int \vec{T}(s) ds + \vec{p}_0, \quad (12)$$

where  $\vec{p}_0$  is the position vector of the start point of the fiber in the laboratory coordinate. Here in Fig. 3(b),  $\vec{p}_0$  is (0 0 0).

## 4. Simulation

The strain along the fiber is numerically obtained through a simulation algorithm called rotation minimizing frame (RMF) which is usually used in computer graphics to model e.g., snakes in a natural way [17]. Here, we use it to construct the fiber shape sensor and obtain the strain along the fiber when bending. The strain can be numerically obtained with a high density. After getting the strain, we sample those strain with a practical sampling spatial interval. Then, the strain is input to the reconstruction algorithm to reconstruct the shape. Through this method we can avoid the influence of error source such as temperature fluctuation and inaccuracy of the sensor assembly and only validate the effect of the reconstruction method. What's more, this method provides a general procedure to numerically simulate and obtain the accurate strain with a curve of the certain shape. By using the RMF, we can change many parameters such as the sample spatial interval, the reconstructed shape, and the configuration of the fiber shape sensor. Next, we will describe our method with two parts. One is fiber distributed strain simulation algorithm RMF and the other one is the fiber shape reconstruction with some different typical curves. Each reconstruction result is evaluated by the deviation from ideal position using Euclidean distance  $\|\vec{p}_0(s) - \vec{p}(s)\|$  at the same position along the shape sensor.  $\vec{p}_0(s)$  is the position vector of the center line of the sensor given by the certain parameter equation.  $\vec{p}(s)$  is the position vector of the reconstructed center line of the sensor.

### 4.1 Fiber Distributed Strain Simulation

For the spatially continuous differentiable curve  $\vec{R}(u) = X(u)\vec{i} + Y(u)\vec{j} + Z(u)\vec{k}$ , where  $u$  represents the length along the curve in 3-D space. The local coordinate system is represented as  $(\vec{r}(u), \vec{s}(u), \vec{t}(u))$ ,  $\vec{t}(u)$  and  $\vec{r}(u)$  are the unit tangent vector and the unit direction vector of the curve respectively.  $\vec{s}(u)$  is defined as  $\vec{s}(u) = \vec{t}(u) \times \vec{r}(u)$ .  $(\vec{r}(u), \vec{s}(u), \vec{t}(u))$  is called the minimum rotation frame (RMF) of a curve. The solving process of the distributed strain along fiber consists of the following three steps.

*Step 1. Calculate the RMF of the center line:* For a given space curve  $\vec{R}(u)$  with a certain parameter equation, the unit tangent vector  $\vec{t}_i(u)$  along the curve can be solved according to

$$\vec{t}_i(u) = \frac{\vec{R}'_i(u)}{\|\vec{R}'_i(u)\|} = \frac{X'(u)\vec{i} + Y'(u)\vec{j} + Z'(u)\vec{k}}{\sqrt{(X'(u))^2 + (Y'(u))^2 + (Z'(u))^2}}. \quad (13)$$

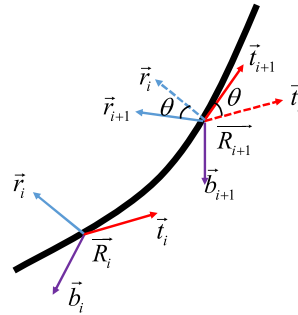


Fig. 4. The graph of RMF in a curve. Two adjacent points are plotted.

The initial value of  $\vec{r}(u)$  is given as  $\vec{r}_0$ . It can be chosen arbitrarily and the direction of  $\vec{r}(u)$  can be used as the direction from the center line to one of the outer fiber cores according to the configuration of the fiber shape sensor on the cross section. Considering the two adjacent sampled points  $\vec{R}_i$  and  $\vec{R}_{i+1}$  on the fiber as shown in Fig. 4, we will demonstrate how to get  $(\vec{r}_{i+1}(u), \vec{s}_{i+1}(u), \vec{t}_{i+1}(u))$  at  $\vec{R}_{i+1}$  through the  $(\vec{r}_i(u), \vec{s}_i(u), \vec{t}_i(u))$  at the last point  $\vec{R}_i$ .  $\vec{R}_i$ ,  $\vec{R}_{i+1}$ ,  $\vec{t}_i$  and  $\vec{t}_{i+1}$  can be calculated according to the given parameter equation of the curve and the Equation (13). Using the *Rodrigue' Rotation Matrix* [18], we rotate  $\vec{r}_i$  around the vector  $\vec{b}_i$  which defined as  $\vec{b}_i = \vec{t}_i \times \vec{t}_{i+1}$  and get  $\vec{r}_{i+1}$ . The rotation angle is  $\theta = \arccos(\vec{t}_i \cdot \vec{t}_{i+1})$ . Repeat the above process to each position on the curve and obtain the  $(\vec{r}(u), \vec{s}(u), \vec{t}(u))$  at all the points on the fiber.

**Step 2. Placing outer fibers:** After step 1, the RMF along the center line of the shape sensor is obtained and  $\vec{r}(u)$  is known at each position. We take the input curve  $\vec{R}(u)$  as the center line vector of the shape sensor representing as  $\vec{R}_{[c]}(u)$ . The position vector of the first outer fiber core is represented as  $\vec{R}_{[1]}(u)$  and calculated by moving every points in the center line in the direction  $\vec{r}(u)$  with a specified distance  $D$ .  $D$  is the distance from the outer fiber to the center line. For the other outer cores, we rotate  $\vec{r}(u)$  around  $\vec{t}(u)$  by  $120^\circ$  and get  $\vec{r}_{120}(u)$ , then move every points in the center line in the direction  $\vec{r}_{120}(u)$  with distance  $D$  and get the second fiber position vector  $\vec{R}_{[2]}(u)$ . Similarly, rotate every point of  $\vec{r}(u)$  around  $\vec{t}(u)$  by  $240^\circ$  and get  $\vec{r}_{240}(u)$ , then move every points in the center line in the direction  $\vec{r}_{240}(u)$  with distance  $D$  and get the third outer fiber core position vector  $\vec{R}_{[3]}(u)$ .

**Step 3. Strain simulation:** In practice, the length of the center core doesn't change when the shape of the sensor changes if the common-mode force such as axis stress is not been considered. While the outer core fiber deviating from the neutral axis will change its length when the shape of sensor changes. As for the outer core fiber, in each segment, the strain can be calculated by its physical definition, i.e., the relative change. So the strain of the segment between the  $j$ -th and  $(j + 1)$ -th points on the  $m$ -th outer fiber is presented as

$$\varepsilon_{mj} = \frac{\Delta l_{jm} - \Delta l_{jc}}{\Delta l_{jc}} = \frac{\|\vec{R}_{[m]}(h(j+1)) - \vec{R}_{[m]}(hj)\| - \|\vec{R}_{[c]}(h(j+1)) - \vec{R}_{[c]}(hj)\|}{\|\vec{R}_{[c]}(h(j+1)) - \vec{R}_{[c]}(hj)\|}. \quad (14)$$

$\Delta l_{jc}$  is the length between the  $j$ -th point and  $(j + 1)$ -th point along the central axis of the optical fiber sensor.  $\Delta l_{jm}$  is the length between the  $j$ -th point and  $(j + 1)$ -th point along the  $m$ -th outer fiber core.  $h$  is the length of the micro-segment between the  $j$ -th and  $(j + 1)$ -th points.  $\Delta l_{jc}$  equals to  $h$  numerically.  $m$  is the number of the outer fiber cores. If there are three outer fiber cores,  $m = 1, 2, 3$ .

**Step 4. Sampling strain along the fiber:** We use step 3 to generate the strain of  $M$  points along the fiber with a uniform interval (in our simulation,  $M$  is 10000.). We can get  $\varepsilon_{mj}$  ( $m = 1, 2, 3; j = 1, 2, 3 \dots N$ ) by sampling the above data (obviously  $N < M$ ).  $N$  is the total number of sampling points along the fiber for the experiment. A typical interval is one centimeter which can be achieved using commercial OFDR sensing system. Then  $\varepsilon_{mj}$  are input to the reconstruction algorithm, i.e., Frenet Frame and Parallel Frame which will be demonstrated in the next part.

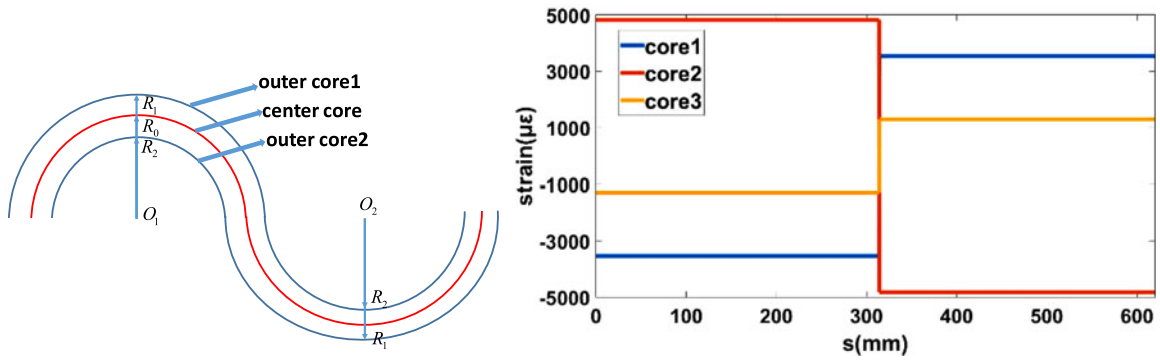


Fig. 5. (a) The configuration and shape to be simulated. Red curve is the center core of the shape sensor. Core 3 is behind the paper and not plotted. (b) The simulated strain in the three outer cores by the RMF method (tensile stress is negative and compressive stress is positive).

To verify the correctness of the above procedure, we simulated the shape sensor of a dual-semicircle as shown in Fig. 5(a). The center line in each part is a semicircle with a diameter of 200 mm. The distance between the outer optical fiber and the center line is 0.5 mm, we simulated the strain of the outer fiber cores using the method mentioned above. Note the core 1 is not located on the maximum deformation surface, it has an angle of  $\pi/4$  with the paper outward direction (so it has a distance of  $0.5 \cos(\pi/4)$  mm from neutral axis). Other cores each has an included angle of  $2\pi/3$  with core 1.

The theoretical strain in each semicircle is calculated by the definition of the strain (the relative change of the length)

$$\varepsilon_{1,2,3} = \frac{\Delta l}{l} = \frac{\pi R_{1,2,3} - \pi R_0}{\pi R_0} \quad (15)$$

From Equation (15) and Fig. 5(a), we can ensure that the strains before and after the border have equal value but opposite sign in each fiber core.

From Fig. 5(b), we can find the simulated strain is constant in each semicircle and has a sudden change in the border of two semicircles. These are coincident with theoretical value. The error is less than 0.0001% compared with the results calculated by the theory of mechanics of materials.

As for the other typical curves, since each local segment can be treated as a semicircle, we think it has the same condition and results with the semicircle we showed above. Even though, we have used the Finite Element Analysis (FEA) software to simulate the typical shapes and found the error is also negligible in each condition. So we believe that the RMF method is feasible.

## 4.2 Validation of the Reconstruction Method

**4.2.1 Curvature-Changing Cylindrical Spiral:** This part aims to compare the reconstruction accuracy of the two reconstruction algorithms when there are no local line or singularities. The curve to be reconstructed in this part is a curvature-changing cylindrical spiral and the bending radius increases linearly with the length of the fiber. The parameter equation of the curve is

$$\begin{cases} X = 100u \times \sin(u) \\ Y = 100u \times \cos(u) \quad (0 \leq u \leq \pi). \\ Z = 100u \end{cases} \quad (16)$$

Three outer fiber cores are symmetrically distributed outside the center line and the distance between the center line to each outer core is set to 0.5 mm. 20 strain points are sampled with an equal interval along three outer 700 mm-long fiber cores and each triplet strain is in the same cross section. The curve is reconstructed using Frenet Frame and Parallel Frame respectively. 50 points are chosen along the fiber to calculate the error. The errors are shown in the Fig. 6. These



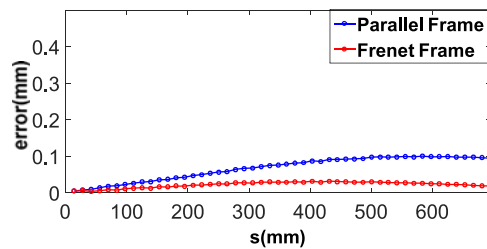


Fig. 6. The error of the reconstructed curvature-changing cylindrical spiral.

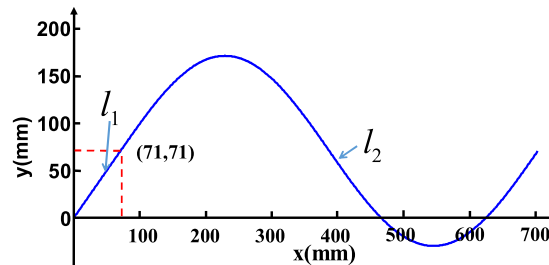


Fig. 7. The shape of the curve to be reconstructed, a 700 mm-long curve combined by a segment of line donated as  $l_1$  and a segment of sinusoidal curve donated as  $l_2$ .

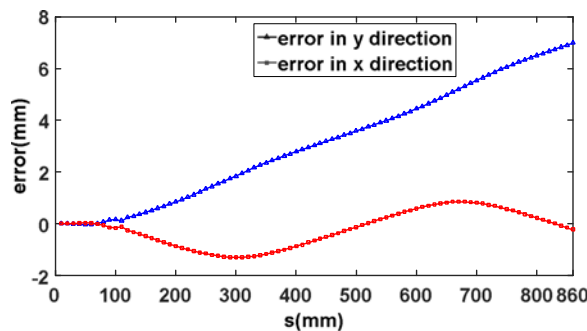


Fig. 8. The error of reconstruction of a curve with a local line segment when using the Parallel Frame. Error components in axis x and y of each position are plotted respectively.

two errors are both negligible which are below 0.015% of the total length. This indicates that the two kinds of reconstruction methods can reconstruct the space curve effectively when there are no local line or singularities in the curve.

**4.2.2 Local Line Segment:** This part investigates the reconstruction effect when the curve exists local line segment. The shape to be reconstructed is shown in Fig. 7. A 700 mm-long curve is combined with a segment of line donated as  $l_1$  and a segment of sinusoidal curve donated as  $l_2$ . The parameter equation of the curve is

$$l_1 : \begin{cases} X = 100u \\ Y = 100u \quad (0 \leq u < 0.71), \\ Z = 0 \end{cases}, \quad l_2 : \begin{cases} X = 100u \\ Y = 100 \sin(u - 0.71) + 71 \quad (0.71 \leq u \leq 6.8). \\ Z = 0 \end{cases} \quad (17)$$

There exist  $\vec{p}''(s) = 0$  in the segment of  $l_1$ . Fiber shape can not be solved by using Frenet frame in the segment  $l_1$ . So only Parallel Frame is used here.

The error is shown in Fig. 8. Parallel Frame has successfully reconstructed the curve with a segment of the line which failed in the reconstruction by Frenet Frame. The error in both directions is below 1% of the total length.

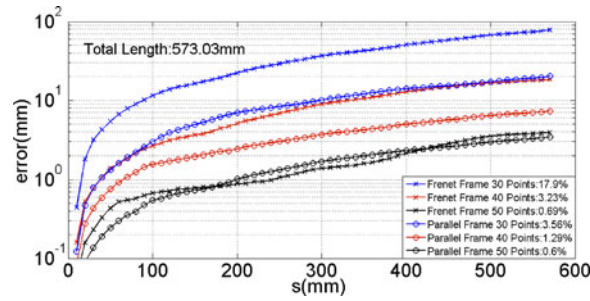


Fig. 9. The error of 2-D multi-period sinusoidal curve using Parallel Frame and Frenet Frame. The percent error of the end point are shown in the bottom right corner.

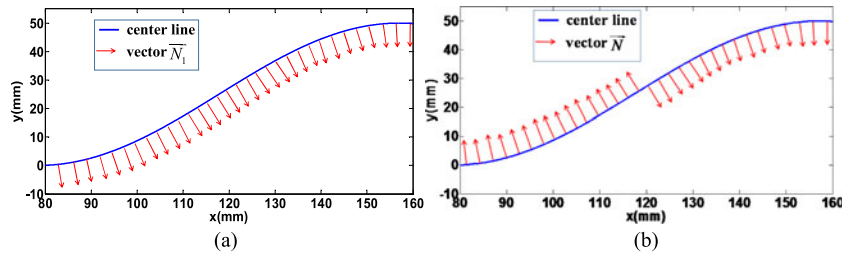


Fig. 10. The character vector of each Frame between 100 mm to 200 mm. (a) Vector  $\vec{N}_1$  in the curve using Parallel Frame. (b) Vector  $\vec{N}$  in the curve using Frenet Frame.

**4.2.3 2-D Multi-period Sinusoidal Curve:** To demonstrate the situation when reconstructing the curve with singularities, a 2-D multi-period sinusoidal curve will be reconstructed in this part. This kind of curve represents the situation that the bending direction changes in the practical situation. The parameter equation is

$$\begin{cases} x = 25u \\ y = 25 \cos(u) \quad (0 \leq u \leq 6\pi). \\ z = 0 \end{cases} \quad (18)$$

The total length of the fiber is 573.03 mm and it is composed of 3 sinusoidal curve periods. 30, 40, 50 strain points are sampled. The error is shown in Fig. 9.

It can be seen from Fig. 9, with the increase of the strain sample number, the error decreases. When the sample strain is up to 50 points, the error is both below 1% of the total length for these two methods. However, when the number of the strain points decreases, the error of the end point of the fiber using Frenet Frame significantly increases compared to Parallel Frame. The error of the distal end is 17.9% reconstructed by Frenet Frame, which is much higher than Parallel Frame which is 3.56% when the number of sample strain is 30 points. This is because the parameters in the Parallel Frame are continuous and have no sudden change when in reconstruction. As shown in Fig. 10(a),  $\vec{N}_1$  is continuous in all curve. While in Frenet Frame, the normal vector  $\vec{N}$  flips on the singularity as shown in Fig. 10(b) and the bending direction angle has step change as shown in the Fig. 11. This lead to the error when interpolation or fitting. What's more, a plane curve with non-vanishing curvature has zero torsion at all points. If the bending direction changes, the torsion will not be zero, making the torsion function not smooth and bringing the error in the solving of Equation (7).

The cubic spline interpolation, which has the advantages of good numerical stability and smooth interpolation curve, is employed to interpolate the coefficient matrix in Equation (7) as [10]. As shown in Fig. 11, the bending direction angle are interpolated using cubic spine in the calculation process of Frenet Frame. When the number of the sampled strain points is less, the fitting accuracy

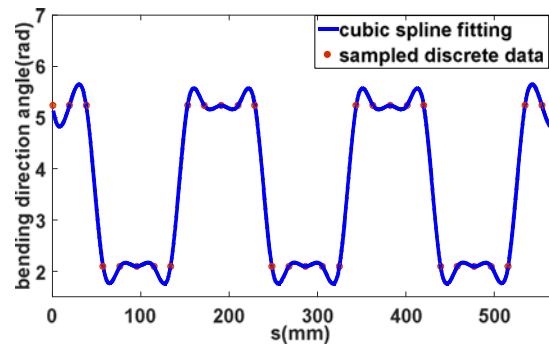


Fig. 11. Bending direction angle and its fitting curve.

at the singularities is worse. So Frenet Frame is more susceptible to the number of sampled strain points. When the number of strain points are less, the reconstruction result by Frenet Frame will have more error.

The reconstruction error comes from mainly four aspects. The first is the error accumulation effect. When in reconstruction, the accuracy of the next point is based on the accuracy of the position of the last point. The second error is from the numerical methods used to solve the ordinary differential equations which was mentioned as well in the reference [19]. The traditional numerical methods such as the Euler method and the 4th order Runge-Kutta tend to be inconsistent to the geometrical characteristics of the three-dimensional space curve, and they also contain a lot of truncation errors from the neglected higher order terms [19]. Hence, space curve reconstruction leads to a very large error with a tremendous loss of orthonormality in the frame. The third is the angle amplification error. If the front shape has a deviation from the correct angle, the curve will point to a wrong direction and have an increasing error with the increasing of the fiber length. The fourth is the number of sampling strain along the fiber. The number of sample points of strain influence both of the reconstruction methods. Duncan *et al.* [20] has demonstrated the relationship between the reconstruction accuracy and the number of strain points based on the Nyquist criteria theory. To a curve rapid variation of curvature, more points of strain need to be sampled.

## 5. Conclusion

In conclusion, the principle and the reconstruction method based on the Parallel Frame are demonstrated in this paper. Parallel Frame has its advantages when a curve to be reconstructed has singularities or line locally. In fact, this is a very common situation in the fiber shape sensing since the fiber usually changes its bending direction in practice. RMF method has been developed and applied to numerically simulate and obtain the ideal strain along each fiber with input shape. Parallel Frame shows more accuracy when the number of sampled strain points is low compared with the Frenet Frame. When the number of sample strain points is 30 along a 573.03 mm-long fiber with 3 sinusoidal curve periods, the error of the distal end is 17.9% for Frenet Frame, much higher than that of Parallel Frame with 3.56%.

Considering the focus of this research is to verify a new reconstruction method, it is thought that our simulation method in this paper is enough to verify our reconstruction method. In the practical shape measurement, the distributed strain has non-negligible error because of the limited accuracy of the interrogation system and the inaccuracy of geometric configuration of the shape sensor. Therefore, the results of practical reconstruction will have more error than current simulation results. The shape reconstruction experiment through the Parallel Frame will be implemented in our future work.

## Appendix Derivation of Equation (10)

According to the literature [21], when the Equation (A1) satisfied ( $i = 1, 2, \dots, M$ .  $M$  is an integer.  $\theta_1$  is a constant),

$$\theta_i = \theta_1 + \frac{2\pi}{M}(i - 1) \quad (\text{A1})$$

the Equation (A2) holds.

$$\begin{aligned} \sum_i^M \cos 2\theta_i &= \frac{\sin \left( M \frac{2\pi}{M} \right) \cos \left( 2\theta_1 + (M - 1) \frac{2\pi}{M} \right)}{\sin \frac{2\pi}{M}} = 0 \\ \sum_i^M \sin 2\theta_i &= \frac{\sin \left( M \frac{2\pi}{M} \right) \sin \left( 2\theta_1 + (M - 1) \frac{2\pi}{M} \right)}{\sin \frac{2\pi}{M}} = 0 \end{aligned} \quad (\text{A2})$$

So (A3) holds.

$$\begin{aligned} \sum_{i=1}^M \cos \left( \theta_b - 2\theta_1 - 2 \times \frac{2\pi(i - 1)}{M} \right) &= \sum_{i=1}^M \cos \left( 2 \times \left( \theta_1 - \theta_b/2 + \frac{2\pi(i - 1)}{M} \right) \right) \\ &= \frac{\sin \left( M \frac{2\pi}{M} \right) \cos \left( 2(\theta_1 - \theta_b/2) + (M - 1) \frac{2\pi}{M} \right)}{\sin \left( \frac{2\pi}{M} \right)} = 0 \end{aligned} \quad (\text{A3})$$

So (A4) holds.

$$\sum_{i=1}^M (\cos(\theta_b - 2\theta_i)) = 0 \quad (\text{A4})$$

Then,

$$\sum_{i=1}^M (\cos(\theta_b - \theta_i) \cos \theta_i + \sin(\theta_b - \theta_i) \sin \theta_i) = 0. \quad (\text{A5})$$

Then,

$$\begin{aligned} \sum_{i=1}^M \cos(\theta_b - \theta_i) \cos \theta_i + \sum_{i=1}^M \sin(\theta_b - \theta_i) \sin \theta_i &= 0 \\ \sum_{i=1}^M \cos(\theta_b - \theta_i) \cos \theta_i + \sum_{i=1}^M \sin(\theta_b - \theta_i) \sin \theta_i \\ 2 \sum_{i=1}^M \cos(\theta_b - \theta_i) \cos \theta_i &= \sum_{i=1}^M \cos(\theta_b - \theta_i) \cos \theta_i - \sum_{i=1}^M \sin(\theta_b - \theta_i) \sin \theta_i \\ 2 \sum_{i=1}^M \cos(\theta_b - \theta_i) \cos \theta_i &= \sum_{i=1}^M (\cos(\theta_b - \theta_i) \cos \theta_i - \sin(\theta_b - \theta_i) \sin \theta_i) \\ 2 \sum_{i=1}^M \cos(\theta_b - \theta_i) \cos \theta_i &= \sum_{i=1}^M \cos(\theta_b - \theta_i + \theta_i) \\ 2 \sum_{i=1}^M \cos(\theta_b - \theta_i) \cos \theta_i &= M \cos \theta_b. \end{aligned} \quad (\text{A6})$$

Then,

$$\frac{2}{M} \sum_{i=1}^M \cos(\theta_b - \theta_i) \cos \theta_i = \cos \theta_b. \quad (\text{A7})$$

Substitute Equation (9) into (A7)

$$\kappa \cos \theta_b = -\frac{2}{M} \sum_{i=1}^M \frac{\varepsilon_i}{r_i} \cos \theta_i \quad (\text{A8})$$

Similarly, we can get

$$\kappa \sin \theta_b = -\frac{2}{M} \sum_{i=1}^M \frac{\varepsilon_i}{r_i} \sin \theta_i. \quad (\text{A9})$$

As for a symmetrically arranged tri-core fiber,  $M = 3$  and the Equation (10) holds.

## References

- [1] Y.-L. Park *et al.*, "Real-time estimation of 3-D needle shape and deflection for MRI-guided interventions," *IEEE/ASME Trans. Mechatronics*, vol. 15, no. 6, pp. 906–915, Dec. 2010.
- [2] X. Yi, J. Qian, Y. Zhang, Z. Zhang, and L. Shen, "3-D shape display of intelligent colonoscope based on FBG sensor array and binocular vision," in *Proc. IEEE Conf. Complex Med. Eng.*, 2007, pp. 14–19.
- [3] E. Lally, M. Reaves, E. Horrell, S. Klute, and M. Froggatt, "Fiber optic shape sensing for monitoring of flexible structures," *Proc. SPIE*, vol. 8345, 2012, Art. no. 83452Y.
- [4] Z. Zhao, M. A. Soto, M. Tang, and L. Thévenaz, "Distributed shape sensing using Brillouin scattering in multi-core fibers," *Opt. Exp.*, vol. 24, no. 22, pp. 25211–25223, 2016.
- [5] S. C. Ryu and P. E. Dupont, "FBG-based shape sensing tubes for continuum robots," in *Proc. IEEE Conf. Robot. Autom.*, 2014, pp. 3531–3537.
- [6] F. Parent *et al.*, "Enhancement of accuracy in shape sensing of surgical needles using optical frequency domain reflectometry in optical fibers," *Biomed. Opt. Exp.*, vol. 8, no. 4, pp. 2210–2221, 2017.
- [7] R. J. Roesthuis, M. Kemp, J. John, and S. Misra, "Three-dimensional needle shape reconstruction using an array of fiber Bragg grating sensors," *IEEE/ASME Trans. Mechatronics*, vol. 19, no. 4, pp. 1115–1126, Aug. 2014.
- [8] J. Bos, J. Klein, E. Sanborn, and D. Gifford, "Fiber optic strain, temperature and shape sensing via OFDR for ground, air and space applications," *Proc. SPIE*, vol. 8876, 2013, Art. no. 887614.
- [9] K. Henken, D. Van Gerwen, J. Dankelman, and J. Van Den Dobbelsteen, "Accuracy of needle position measurements using fiber Bragg gratings," *Minimally Invasive Therapy Allied Technol.*, vol. 21 no. 6, pp. 408–414, 2012.
- [10] J. P. Moore and M. D. Rogge, "Shape sensing using multicore fiber optic cable and parametric curve solutions," *Opt. Exp.*, vol. 20, no. 3, pp. 2967–2973, 2012.
- [11] H. Pauer, C. Ledermann, and H. Woern, "Motivation of a new approach for shape reconstruction based on FBG-optical fibers: Considering of the Bragg-gratings composition as a sensor network," in *Proc. IEEE Int. Conf. Intell. Sens. Sens. Netw. Inf. Process.*, 2014, pp. 1–5.
- [12] H. Moon, J. Jeong, S. Kang, K. Kim, Y.-W. Song, and J. Kim, "Fiber-Bragg-grating-based ultrathin shape sensors displaying single-channel sweeping for minimally invasive surgery," *Opt. Lasers Eng.*, vol. 59, pp. 50–55, 2014.
- [13] M. D. Todd, C. J. Stull, and M. Dickerson, "A local material basis solution approach to reconstructing the three-dimensional displacement of rod-like structures from strain measurements," *J. Appl. Mech.*, vol. 80, no. 4, 2013, Art. no. 041028.
- [14] A. J. Hanson, "Quaternion Frenet frames: Making optimal tubes and ribbons from curves," Indiana Univ., Bloomington, IN, USA, Tech. Rep. TR-407, 1994.
- [15] R. L. Bishop, "There is more than one way to frame a curve," *Amer. Math. Monthly*, vol. 82, no. 3, pp. 246–251, 1975.
- [16] A. J. Hanson and H. Ma, "Quaternion frame approach to streamline visualization," *IEEE Trans. Vis. Comput. Graph.*, vol. 1, no. 2, pp. 164–174, Jun. 1995.
- [17] W. Wang, B. Jüttler, D. Zheng, and Y. Liu, "Computation of rotation minimizing frames," *ACM Trans. Graph.*, vol. 27, no. 1, 2008, Art. no. 2.
- [18] E. Piña, "Rotations with Rodrigues' vector," *Eur. J. Phys.*, vol. 32, no. 5, pp. 1171–1175, 2011.
- [19] L. Sungyeop and S. Han, "Helical extension method for solving the natural equation of a space curve," *Surf. Topogr., Metrol. Properties*, vol. 5, no. 3, pp. 035002–035015, 2017.
- [20] R. G. Duncan *et al.*, "High-accuracy fiber-optic shape sensing," *Proc. SPIE*, vol. 6530, 2007, Art. no. 65301S.
- [21] M. D. Rogge and J. P. Moore, "Shape sensing using a multi-core optical fiber having an arbitrary initial shape in the presence of extrinsic forces," U.S. Patent 8 746 076, 2014.